# Chunk mixing implosion experiments using deuterated foam capsules with gold dopant

Yudong Pu,[1] Xuan Luo,[1] Lu Zhang,[1] Chuankui Sun,[1] Zhimin Hu,[1] Gang Shen,[2] Xuerong Wang,[2] Qi Tang,[1] Zhen Yuan,[1] Feng Wang,[1] Dong Yang,[1] Jiamin Yang,[1] Shaoen Jiang,[1] Yongkun Ding,[2] and Jianguo Wang[2]

[1]*Laser Fusion Research Center, China Academy of Engineering Physics, Mianyang, Sichuan 621900, China*

[2]*Institute of Applied Physics and Computational Mathematics, Beijing 100088, China*

(Received 13 April 2019; revised 22 July 2020; accepted 23 July 2020; published 13 August 2020)

To study the effects of chunk mixing, the implosion experiments using capsules filled with deuterated foam (CDF capsule) were carried out on the Shenguang laser facility. Three types of the CDF capsules, namely the capsules without Au dopant, with micrometer Au dopant, and with atomic Au dopant, were used in the experiments. The neutron yields, the size, and the emission intensity of the hotspots were measured. The CDF capsules without Au dopant produced the highest neutron yield and the largest hotspot size at the time of peak emission. The capsules with micrometer or atomic Au dopant showed similar reduced neutron yield and hotspot size. The time-resolved hotspot emissions showed different behaviors between different capsules. One-dimensional simulations were carried out to understand the implosion dynamics of the CDF capsule without Au dopant, and to provide the thermodynamic conditions that the Au dopant would experience during the implosion. The effects of Au dopant were then discussed qualitatively.

DOI: 10.1103/PhysRevE.102.023204

## I. INTRODUCTION

Mixing between shell material and gas fuel, caused by hydrodynamic instability [1–3], isolated defects [4–6], or kinetic effects [7–9], is the key to understanding the degradation of implosion performance in the research of inertial confinement fusion (ICF) [10–13]. There are theoretical and experimental studies to quantify the effects of mixing providing the shell material is atomically presented in the gas fuel at the beginning of the implosion [14–18]. There are also studies to quantify the effects of subgrid mixing by using the Reynolds averaged Navier-Stokes equations (RANS) model to explain the 14-MeV neutron yields [19–21]. In all these studies, the mixing between the shell and gas are treated as atomic mixing. However, it is known that the length scale resulting from the growth of hydrodynamic instability spans from the dimension of the system to the scale of viscosity dissipation [22,23]. It is interesting to know the role played by the mesoscale at the interface during the implosion. The spikes may be described as "chunky" when certain places inside the spikes cannot be reached by certain particles. For example, if an electron process is involved, the spike is chunky when the electron collisional mean free path is smaller than the spike dimensions, and if the radiations process is involved, the spike is chunky when the radiation mean free path is smaller than the spike dimensions. Otherwise, the spikes could be treated by atomic mixing. The complexity of chunk mixing lies in the continually evolving thermodynamic conditions of the spikes under extreme conditions of high-energy density and high Mach number. The processes of electron and radiative heating, diffusion, expansion, and shearing work together and competitively to change the thermodynamic conditions and decrease the dimension of the spikes. The nature of multiscale and complex evolution makes the chunk mixing hard to simulate. To the authors' knowledge, there are few codes capable of modeling chunk mixing in the context of ICF implosion. In addition, there are few experiments devoted to the effects of chunking mix on implosion performance. The only example of such study is the "Marble Campaign" carried out at the National Ignition Facility [24]. The capsules with finer pores are expected to be less chunky, and produce more 14-MeV neutrons. In our work, the capsules with CH ablators is also filled with deuterated foam. Instead of filling $H_2/T_2$ mixture, the gold dopant is distributed inside the deuterated foam with the same weight fraction but different initial size. It is expected that the gold grains with smaller diameters would be less chunky, and should act more like atomic mixing. The neutron yield should also change accordingly with the dimensions of the Au dopant. In this article, we report the comparative studies of implosion experiments using the capsules without Au dopant, with micrometer Au dopant, and with atomic Au dopant. The experimental observations would be helpful to test the model describing the effects of chunk mixing in ICF implosion.

## II. TARGETS AND DIAGNOSTICS

The experiments are carried out on the Shenguang laser facility [25]. 64-kJ laser energy in a 1.6-ns squared pulse is used to create a thermal radiation field of 250 eV. The capsule is driven by the radiation field. The capsules are deuterated foam balls overcoated with plastic ablator. The diameter of the foam ball is 720 $\mu$m. The thickness the plastic ablator is 40 $\mu$m, as shown in Fig. 1. The type-I capsule is not doped with Au. It is a reference target. The type-II capsule is doped with Au particles. The weight fraction of the Au particles is 8%, and the average diameter of the Au particles is 1 $\mu$m. The Au particles are uniformly distributed in the deuterated foam ball. The type-III capsule is doped with atomic Au. The Au weight fraction of the type-III capsule is the same as that of the

 

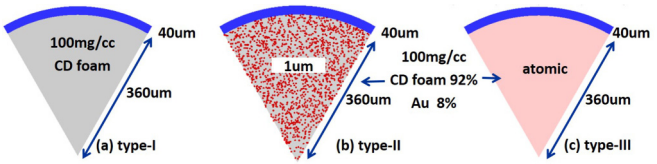


FIG. 1. Schematic of reference target (a), type I, target with micrometer Au dopant (b), type II, and target with atomic Au dopant (c), type III.

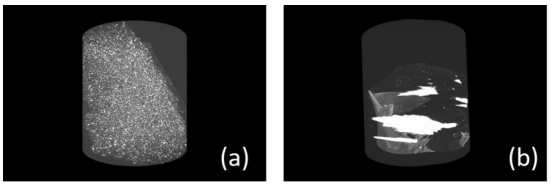


FIG. 2. X-ray images of deuterated foam samples doped with micrometer Au (a) and atomic Au (b).

type-II capsule. The deuterated foams are analyzed on an ICP (inductively coupled plasma-atomic emission spectrometry) element analyzer. The amount of element is determined by quantitative analysis of special emission spectra intensity. The measured foam density and Au weight fraction are shown in Table I. Information concerning the morphology and gold distribution in the deuterated foam materials was obtained from Scanning Electron Micrography (SEM), which was equipped with an EDX (energy dispersive x-ray spectroscopy). EDX is widely used to determine the atomic composition of materials and impurities nondestructively. The deuterated foam is also characterized using computerized tomography (CT) scans with submicrometer spatial resolution. The reconstructed x-ray images of Au doped foam samples are shown in Fig. 2. In Fig. 2(a), the small bright spots represent the doped micrometer Au grains. In Fig. 2(b), a bright spot is hardly seen which indicates a distinct initial condition of the micrometer doped foam. The white areas seen in Fig. 2(b) are the boundary of the sample or the cracks inside the sample.

The neutron yield is measured using a scintillator detector. The implosion emission is measured using a flat crystal coupled to an x-ray streak camera. The spectra are recorded with ~20-eV spectral and 30-ps temporal resolution. The implosions are viewed through 25-$\mu$m CH patches on the hohlraum with an additional 200-$\mu$m Be and 5-$\mu$m Al filtering at the spectrometer. The measured spectral energy is designed between 3 and 4 keV aiming to record the *M*-band emission of the gold dopant. To eliminate the influence of the Au emissions near the laser entrance holes, a slit is used to limit the view field of the streak camera, and shields are also mounted near the laser entrance holes. The hotspot shape is measured by an x-ray framed camera with ~15-$\mu$m spatial and 70-ps temporal resolution [26]. The diagnostic window is on the waist of the hohlraum and covered with 25-$\mu$m CH film. The images are filtered by 200-$\mu$m Be and 20-$\mu$m Al.

TABLE I. Measured density and Au weight fraction of deuterated foam.

| Sample | $\rho$(mg/cm$^3$) | Amount of Au (wt%) |
|---|---|---|
| Micrometer Au | 104.82 | 8.67 |
| Atomic Au | 109.26 | 8.15 |
| Undoped | 106.43 | |

## III. EXPERIMENTAL RESULTS

### A. Neutron yield

The neutron yields are shown in Fig. 3. There is a repeated shot for each kind of capsule. The variations of neutron yields between shots of the same type of capsule are much smaller than the variations between shots of different type of capsules.

### B. Hotspot images

The hotspot images are shown at two specific times, namely the x-ray bang time (Fig. 4) and 160 ps before x-ray bang time (Fig. 5). In Fig. 4, the contours of 50% peak intensity are also shown. The radii of the contours were 31, 15, and 17 $\mu$m for the type-I, type-II, and type-III capsules respectively. In Fig. 5, a halo around the central bright hotspot is clearly seen for the type-III capsule at 160 ps before the x-ray bang time. This time is just after the converging shocks colliding at the capsule center. The central bright spots are not observed before this time.

### C. Time-resolved implosion emission

The typical result of the streaked spectrum is shown in Fig. 6(a). By integrating the streaked spectrum over photon energy, the time-resolved implosion emission is obtained, as shown in Fig. 6(b). For the type-I capsule, the emission intensity increased monotonically to its peak value. However, for the type-II and type-III capsules, the emission intensities rose at early times, and increased to their peak value sharply just before the x-ray bang time. The early increase of the emission intensities for the doped capsule may be correlated to

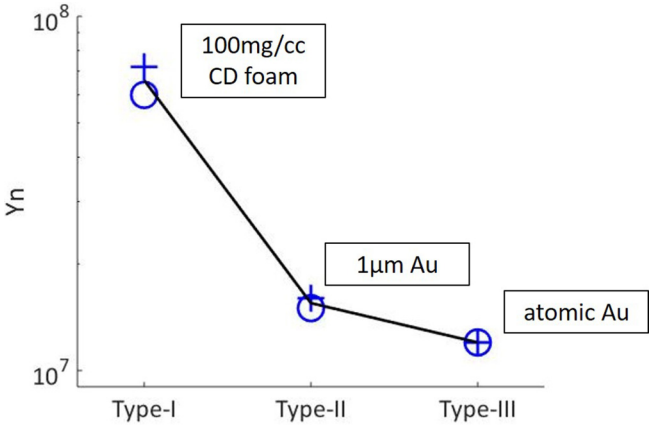


FIG. 3. Measured neutron yields for different types of capsules.

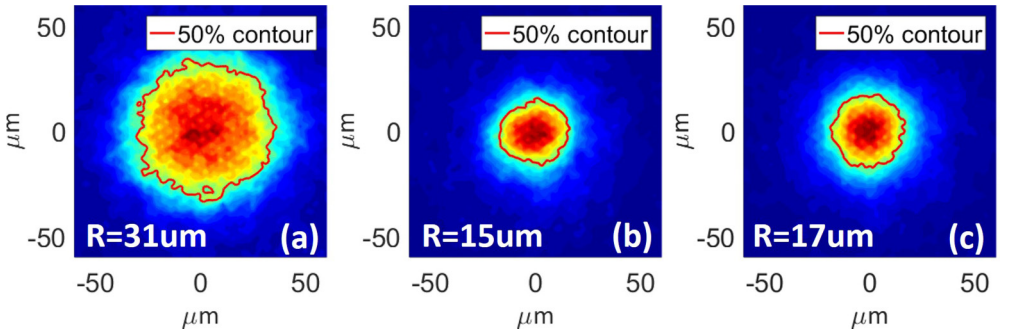


FIG. 4. Intensity normalized hotspot images at x-ray bang time for (a) type-I capsule, (b) type-II capsule, and (c) type-III capsule

the halo observed in the framed images of the type-III capsule (see Fig. 5).

The spectra for different capsules at different times are shown in Fig. 7. Each of the spectra is integrated over a 200-ps interval. The spectrum of the type-I capsule is expected to be the bremsstrahlung spectrum without lines or edges. However, the measured spectrum of the type-I capsule has complex structures. Some of the structures are seen in all shots with fixed locations and repeated patterns despite different capsules have been used. These structures can be attributed to the defects on the cathode. The cathode is not changed during the period of the experiments. It is difficult to make a distinction between the spectral characteristics and the false signals caused by the defects on the cathode. Therefore, the detailed spectral information is uncertain, but the large-scale spectral features and relative intensities between different capsules are still meaningful. It is found that all spectra showed similar shapes and intensities before 0.4 ns, and between 0.4 and 1.2 ns the intensity of the doped capsule exceed the intensity of the type-I capsule while the profiles are still similar. After 1.2 ns, the type-III capsule shows the most intensive radiation. Before the x-ray bang time, the intensity of the type-I capsule increases fast enough and finally exceeds that of the type-II capsule.

## IV. SIMULATION

### A. 1D simulation for the type-I capsule

One-dimensional (1D) radiative-hydrodynamic simulation is carried out for the type-I capsule using the Multi-1D code [27]. The measured target parameters and radiation temperature are used in the simulation. The equation of state and the opacity of the CH material are used for the deuterated foam. The property of being porous of the foam is not considered in the simulation. The neutron yield is calculated by replacing the hydrogen ions with the deuterium ions. The predicted bang time is defined as the time of peak nuclear reaction rate, namely the neutron bang time. Generally, the x-ray bang time was about tens of ps later than the neutron bang time. The radius of the hotspot ($R_{\mathrm{HS}}$) in the simulation is found as the 1-keV temperature contour at the neutron bang time. The comparison between the measurements and the 1D predictions is listed in Table II. The agreement is acceptable.

### B. 0D model for the type-III capsule

1D codes could be also used to describe the implosion dynamics of the atomic doped capsule if the equation of state and the opacity of the mixed material are available. However, for the purpose of qualitative understanding, a zero-dimensional model is developed to describe the energy balance of the hotspot. The price is that the spatial profiles of the temperature and density in the hotspot are lost.

The basic assumption of the 0D model is that the nuclear reaction region with constant mass is treated with uniform temperature, density, and pressure. When atomic Au is added into the foam, the radiation loss is increased significantly, while the heat flux and the pressure at the boundary of the nuclear reaction region are assumed to be little changed. The energy balance of the nuclear reaction region is described by

$$\frac{dE_e}{dt} + \frac{dE_i}{dt} = -\frac{dE_{\mathrm{kin}}}{dt} - p\Delta V + q_e S + P_{\mathrm{rad}}, \qquad (1)$$

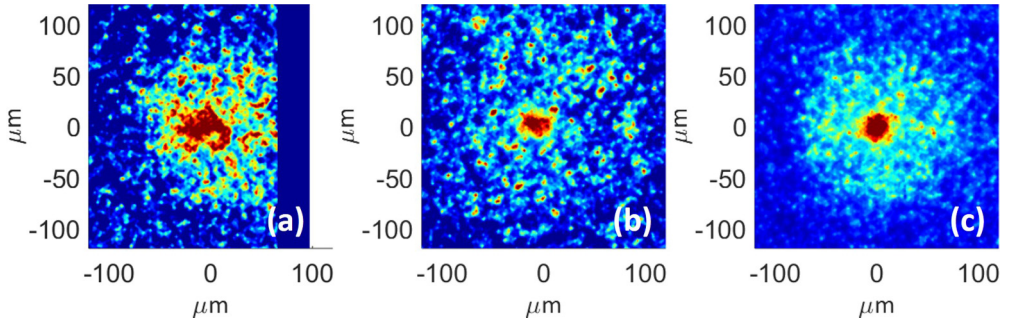


FIG. 5. Intensity normalized hotspot images at 160 ps before x-ray bang time for (a) type-I capsule, (b) type-II capsule, and (c) type-III capsule.

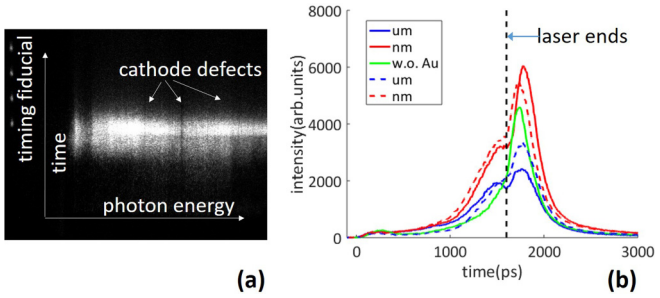


FIG. 6. Typical streaked spectrum (a) and time-resolved implosion emission (b)

where $E_e$ is the electron internal energy, $E_i$ is the ion internal energy, $E_{kin}$ is the kinetic energy, $P$ is the pressure at the interface, $S$ is the area of the interface, $q_e$ was the electron heat flux across the interface, $P_{rad}$ is the radiation power summed over the nuclear reaction region, and $\Delta V$ is the volume change of the nuclear reaction region. $E_e$, $E_i$, and $E_{kin}$ are in units of J. Equation (1) is actually an expression of energy conservation. The initial values of the terms in Eq. (1) are derived from the 1D simulation discussed in previous part of this section. However, the radiative loss term has to be modified to include the effect of gold dopant, while the kinetic-energy term and the internal energy distribution between electrons and ions is assumed the same. The radiative loss term is given by

$$P_{rad}(\mathrm{J\,s^{-1}}) = \int \eta_\upsilon \rho d\upsilon dV, \tag{2}$$

where $\eta_\upsilon$ is the spectral emission coefficient, $\rho$ is the mass density, and $\upsilon$ is the photon frequency. Assuming the LTE

TABLE II. Comparison between measurements and 1D predictions.

| | Yn | Bang time (ns) | $R_{HS}$ ($\mu$m) |
|---|---|---|---|
| Measurement | $6.0 \times 10^7$ | 1.74 (x ray) | 31 (50% contour) |
| 1D simulation | $5.1 \times 10^7$ | 1.71 (neutron) | 35 (1 keV contour) |

condition is satisfied and using Kirchhoff's law, Eq. (2) can be written in terms of Planck mean opacity,

$$P_{rad}(\mathrm{J\,s^{-1}}) = m_{CD}\frac{2\pi^4(kT)^4}{15h^3c^2}K^P_{CD}(T_{CD},\rho_{CD}) + m_{Au}\frac{2\pi^4(kT)^4}{15h^3c^2}K^P_{Au}(T_{Au},\rho_{Au}), \tag{3}$$

where $m_{CD}$ is the mass of the deuterated foam in the nuclear reaction region, $m_{Au}$ is the mass of atomic Au in the nuclear reaction region, $c$ is the speed of light, $h$ is the Planck constant, $K^P_{CD}$ ($\mathrm{cm^2/g}$) is the Planck mean opacity of the deuterated foam, and $K^P_{Au}$ is the Planck mean opacity of the gold. Both $K^P_{CD}$ and $K^P_{Au}$ depend on the material temperature and density, and the dependence can be found in the literature [28]. For simplicity, the opacity of $C$ is used instead of the opacity of CD foam. It is assumed that the Au dopant has equilibrated in temperature and pressure with the environmental CD plasma. The temperature of the gold is equal to the temperature of the foam plasma $T_{Au} = T_{CD}$, and the density of the gold is determined by pressure equilibrium

$$\rho_{Au} = \frac{M_{Au}(1+Z_{CD})}{M_{CD}(1+Z_{Au})}\rho_{CD}, \tag{4}$$

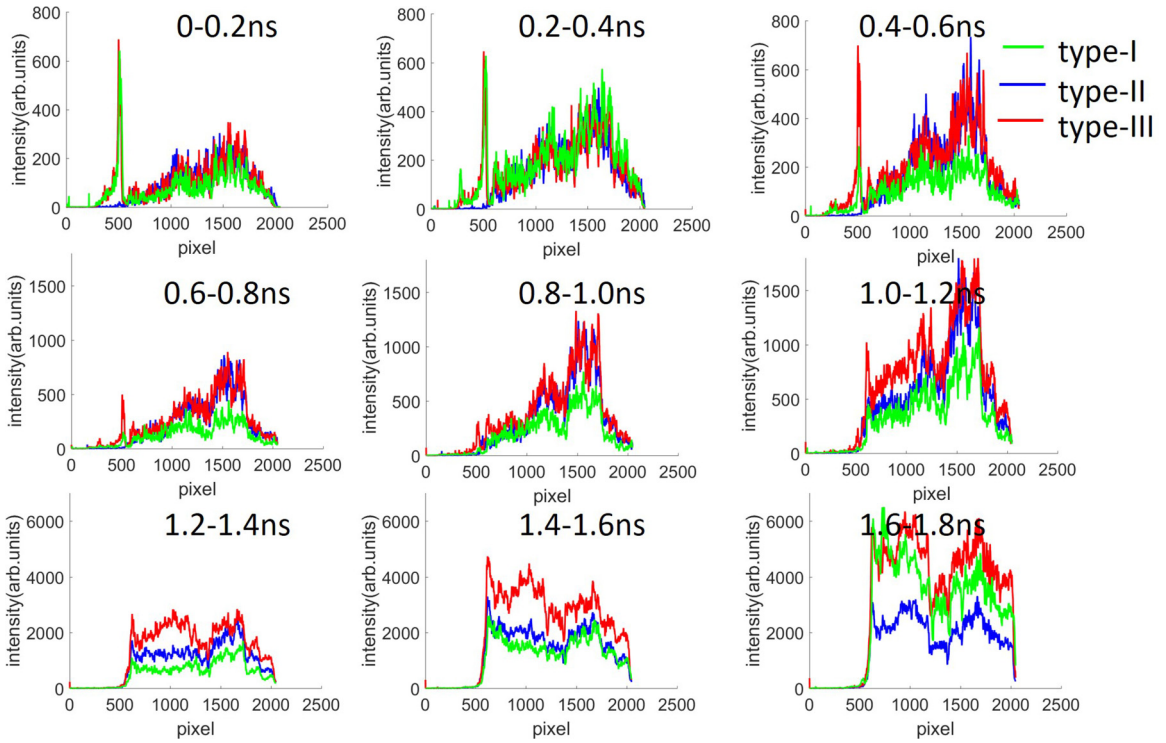


FIG. 7. Spectra for different capsules at different times.

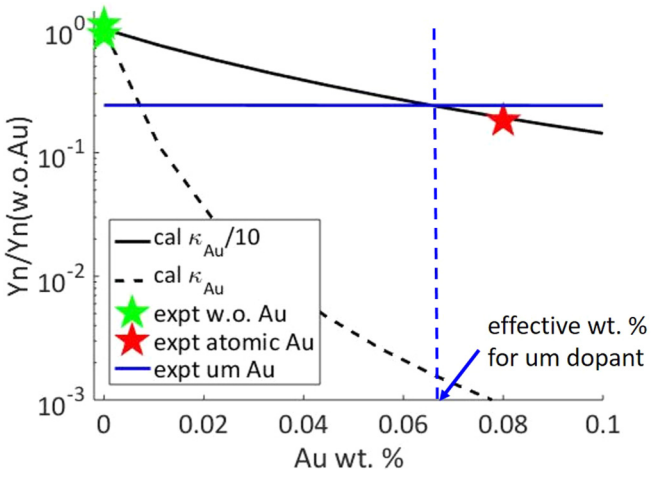


FIG. 8. Normalized neutron yield varies with Au weight fraction (wt%). The black lines are the calculations with (black solid) and without (black dashed) ten times reduction of Au opacity. The measured neutron yield for the type-II capsule is the blue solid line. The intersection between the blue solid line and the black solid line corresponds to the effective weight fraction for the type-II capsule.

where $M_{CD}$ and $M_{\rm Au}$ are the atomic weight, and $Z_{CD}$ and $Z_{\rm Au}$ are the average ionization degree. Finally, inserting the analytical expressions of $K^P_{CD}$ and $K^P_{\rm Au}$ into Eq. (3), and normalizing the term of gold emission to the term of deuterated foam emission, the radiation power is given by

$$P_{\rm rad}({\rm J\,s^{-1}}) = P^{CD}_{\rm rad}\left[1 + 155 \times \frac{f}{(1-f)}\left(\frac{M_{\rm Au}(1+Z_{CD})}{M_{CD}(1+Z_{\rm Au})}\right)^{0.4} \times \rho_{CD}({\rm g/cc})^{-0.6} T_{CD}({\rm keV})^{0.9}\right], \quad (5)$$

where $P^{CD}_{\rm rad}$ is the radiation power of the deuterated foam plasma, and $f$ is the weight fraction of the atomic gold. The second term in the square bracket quantifies the enhancement of the radiation power due to the presence of atomic gold dopant.

The predicted neutron yields with various weight fraction of atomic Au dopant are plotted in Fig. 8 (back dashed line). The calculated neutron yield reduction is larger than expected. The effects of radiative loss must be overestimated. In order to bring the calculation close to the observation, the gold opacity has been reduced by a factor of 10, and the new calculaiton with the reduced gold opacity is shown in Fig. 8 as the solid black line. As predicted by this calculation, the internal energy inside the nuclear reaction region decreases about 30%, and the radiation power increases about 46% at the neutron bang time. The measured neutron yield for the type-II capsule is aslo shown in Fig. 8 as the solid blue line. This line intersects with the solid black line at certain weight fraction. This weight fraction is regarded as the effective weight fraction for type-II capusle.

### C. Discussion for the type-II capsule

In this section, we estimate the characteristic scales of individual process that may affect the evolution of the gold particles in order to shed light on the dominated mechanism of chunk to atomic transition. As we have known from the 1D simulation of the type-I capsule, the nuclear reactions take place in a small central region when the converging shock has collided in the center and rebounced outward. The shock runs faster in the foam than in the gold particle, so it would take more time for the shock to pass through the gold grains. During the time of shock running through the gold grains, the foam has already been shock heated, and begins to heat the gold grains via electron heat conduction. The shock interacting time with the gold particle, defined as the diameter of the particle divided by the shock velocity, is estimated using the model of shock interacting with a boundary [29] and the ideal equation of state. It is found that the shock interaction time is about 5.4 ps, which is much shorter than the nuclear reaction time 30 ps. The gold particles are compressed to 77.2 g/cc with a pressure of 4.9 Gbar and temperature of 300 eV. The density is four times solid density, and the temperature caused the ionization degree is consistent with the pressure given by the Hugoniot condition.

It has been shown in the following that by shock heating alone the radiation loss power of the gold grains is smaller than the radiation loss power of the foam plasma, and the gold grains have little effect on the hotspot energy balance at this stage. The Planck mean opacity of gold at 300 eV and 77.2 g/cc is $1.1 \times 10^4\,{\rm cm^2/g}$, and the mean free path is $1.1 \times 10^{-2}\,\mu$m which is much smaller than the dimension of the gold grains. Therefore, the radiation is trapped inside the gold grains. The radiation loss caused by the optically thick gold grains is roughly equal to $\sigma T^4 * S * N$ in which $S$ is the surface area of the gold grains, and $N$ is the total number of the gold grains in the nuclear reaction region. The radiation loss power is $5.5 \times 10^9\,{\rm J/s}$ which is much smaller than the radiation loss power of the foam plasma $2.4 \times 10^{11}\,{\rm J/s}$.

After the shock passage, the gold grains evolve toward the temperature and pressure equilibrium with the foam. The pressure equilibration is achieved by running a rarefaction wave into the gold grains. The adiabatic sound velocity is $\gamma P/\rho$, and equals $c_s = 1 \times 10^7\,{\rm cm/s}$, and the pressure equilibration time is on the order of 5 ps. Providing the temperature remains 300 eV inside the gold grains during this very short pressure equilibration time, the density drops to 20.5 g/cc by hydrodynamic expansion. At this time, the Planck mean free path is $7.2 \times 10^{-2}\,\mu$m which is still much smaller than the dimension of the gold grains. The radiation is still trapped inside the gold grains.

However, the gold grains are continually heated by the surrounding foam plasma via electron heat conduction, and the heated portion of the gold grains continually expands further to keep the pressure equilibrium. Assuming the temperature of the heated portion of the gold grains is the same as the temperature of the foam, the density of heated gold is determined by Eq. (6) where $P_{CD}$ is the pressure of the foam plasma, $Z$ is the average ionization degree of the heated gold plasma, $N_{\rm A}$ is the Avogadro number, and $M_{\rm Au}$ is the atomic weight of gold;

$$\frac{\rho_{\rm Au}}{M_{\rm Au}} N_A[1 + Z(T_{CD}, \rho_{\rm Au})]kT_{CD} = P_{CD}. \quad (6)$$

The dependence of ionization degree on temperature and density for gold plasma is approximated by the fitted formula

$Z = 59.2 \times T\,(\mathrm{keV})^{0.47}\rho(\mathrm{g/cc})^{-0.02}$. It is found that the density of the heated gold is reduced to 5.1 g/cc. As a result, the Planck mean free path is increased to 2.74 $\mu$m which is larger than the dimension of the gold grains. At this time, the radiation from the gold plasma could escape from the hotspot, bring the internal energy away, and finally quench the thermal nuclear reaction.

## V. CONCLUSION

The implosion experiments using the capsules filled with deuterated foam are carried out at the SG laser facility. Three types of capsules are used in the experiments. The type-I capsule is the reference target. The type-II and type-III capsules are the gold-doped capsules. The weight fraction of the gold dopant is the same for both types. However, the initial size of the gold dopant is different. The type-II capsule is initially with chunky dopant, while the type-III capsule is initially with atomic dopant. The experimental observations are repeatable and changed with the types of the capsule. The implosion dynamics of the type-I capsule is captured by the one-dimensional simulation. The agreements between measurements and calculations are fairly good for the type-I capsule. The 0D model is developed to understand the reduction of the neutron yield caused by the atomic gold dopant. By adjusting the gold opacity used in the 0D model, the correct normalized neutron yield for the type-II capsule has been predicted. The effective weight fraction for the type-II capsule is deduced. As for the type-II capsule, estimations about characteristic scales are discussed. A scenario describing the evolution of the gold particles during the implosion process is proposed. First, the gold particles are heated by the converging and rebounded shocks, and then by electron heat conductions. The process of temperature equilibrium between the gold and foam plasmas gradually increased the gold temperature, while the process of pressure equilibrium between the gold and foam plasmas gradually lowered the gold density. Only when the gold plasma became optically thin could the radiation escape from the hotspot.

However, the mentioned 1D simulation, 0D model, and the scenario for the gold particles could not explain the features observed from the framed hotspot images and the streaked spectra. There is a lack of unified simulation to explain all the observations self-consistently. In other words, the experiments presented in this work can serve as a comprehensive data set to validate this unified simulation.

## ACKNOWLEDGMENTS

The authors would like to thank for financial support the National Key R&D Program of China (Grants No. 2017YFA0403300 and No. 2017YFA0403200) and the National Natural Science Foundation of China (Grants No. 11775201 and No. 91852207).

[1] J. D. Kilkenny, S. G. Glendinning, S. W. Haan, B. A. Hammel, J. D. Lindl, D. Munro, B. A. Remington, and S. V. Weber, A review of the ablative stabilization of the Rayleigh-Taylor instability in regimes relevant to inertial confinement fusion, Phys. Plasmas **1**, 1379 (1994).

[2] D. K. Bradley, D. G. Braun, S. G. Glendinning, M. J. Edwards, J. L. Milovich, C. M. Sorce, G. W. Collins, S. W. Haan, R. H. Page, and R. J. Wallace, Very-high-growth factor planar ablative Rayleigh-Taylor experiments, Phys. Plasmas **14**, 056313 (2007).

[3] V. A. Smalyuk, M. Barrios, J. A. Caggiano, D. T. Casey, C. J. Cerjan, D. S. Clark, M. J. Edwards, J. A. Frenje, M. Gatu-Johnson, V. Y. Glebov *et al.*, Hydrodynamic instability growth and mix experiments at the National Ignition Facility, Phys. Plasmas **21**, 056301 (2014).

[4] I. V. Igumenshchev, F. J. Marshall, J. A. Marozas, V. A. Smalyuk, R. Epstein, V. N. Goncharov, T. J. B. Collins, T. C. Sangster, and S. Skupsky, The effects of target mounts in direct-drive implosion on OMEGA, Phys. Plasmas **16**, 082701 (2009).

[5] P. A. Bradley, J. A. Cobble, I. L. Tregillis, M. J. Schmitt, K. D. Obrey, V. Glebov, S. H. Batha, G. R. Magelssen, J. R. Fincke, S. C. Hsu *et al.*, Role of shocks and mix caused by capsule defects, Phys. Plasmas **19**, 092703 (2012).

[6] N. E. Lanier, J. Workman, and R. L. Holmes, Highly resolved measurements of defect evolution under heated-and-shocked conditions, Phys. Plasmas **14**, 056314 (2007).

[7] M. J. Rosenberg, H. G. Rinderknecht, N. M. Hoffman, P. A. Amendt, S. Atzeni, A. B. Zylstra, C. K. Li, F. H. Séguin, H. Sio, M. G. Johnson, J. A. Frenje, R. D. Petrasso, V. Y. Glebov, C. Stoeckl, W. Seka, F. J. Marshall, J. A. Delettrez, T. C. Sangster, R. Betti, V. N. Goncharov *et al.*, Exploration of the Transition from the Hydrodynamiclike to the Strongly Kinetic Regime in Shock-Driven Implosion, Phys. Rev. Lett. **112**, 185001 (2014).

[8] H. G. Rinderknecht, H. Sio, C. K. Li, A. B. Zylstra, M. J. Rosenberg, P. Amendt, J. Delettrez, C. Bellei, J. A. Frenje, M. Gatu Johnson, F. H. Séguin, R. D. Petrasso, R. Betti, V. Y. Glebov, D. D. Meyerhofer, T. C. Sangster, C. Stoeckl, O. Landen, V. A. Smalyuk, S. Wilks *et al.*, First Observations of Nonhydrodynamic Mix at the Fuel-Shell Interface in Shock-Driven Inertial Confinement Implosions, Phys. Rev. Lett. **112**, 135001 (2014).

[9] H. G. Rinderknecht, M. J. Rosenberg, C. K. Li, N. M. Hoffman, G. Kagan, A. B. Zylstra, H. Sio, J. A. Frenje, M. Gatu Johnson, F. H. Séguin, R. D. Petrasso, P. Amendt, C. Bellei, S. Wilks, J. Delettrez, V. Y. Glebov, C. Stoeckl, T. C. Sangster, D. D. Meyerhofer, and A. Nikroo, Ion Thermal Decoupling and Species Separation in Shock-Driven Implosion, Phys. Rev. Lett. **114**, 025001 (2015).

[10] S. L. Pape, L. F. Berzak Hopkins, L. Divol *et al.*, Fusion Energy Output Greatere than the Kinetic Energy of an Imploding Shell at the National Ignition Facility, Phys. Rev. Lett. **120**, 245003 (2018).

[11] J. Lindl, Development of the indirect-drive approach to inertial confinement fusion and the target physics basis for ignition and gain, Phys. Plasmas **2**, 3933 (1995).

[12] J. D. Lindl, P. Amendt, R. L. Berger, S. G. Glendinning, S. H. Glenzer, S. W. Haan, R. L. Kauffman, O. L. Landen, and L. J. Suter, The physics basis for ignition using indirect-drive

targets on the National Ignition Facility, Phys. Plasmas **11**, 339 (2004).

[13] J. Lindl, O. Landen, J. Edwards, E. Moses, and NIC Team, Review of the National Ignition Campaign 2009–2012, Phys. Plasmas **21**, 020501 (2014).

[14] N. C. Woolsey, B. A. Hammel, C. J. Keane, C. A. Back, J. C. Moreno, J. K. Nash, A. Calisti, C. Mossé, R. Stamm, B. Talin *et al.*, Competing effects of collisional ionization and radiative cooling in inertially confined plasmas, Phys. Rev. E **57**, 4650 (1998).

[15] D. C. Wilson, G. A. Kyrala, J. F. Benage Jr., F. J. Wysocki, M. A. Gunderson, W. J. Garbett, V. Y. Glebov, J. Frenje, B. Yaakobi, H. W. Herrman *et al.*, The effects of pre-mix on burn in ICF capsules, J. Phys.: Conf. Ser. **112**, 022015 (2008).

[16] A. R. Miles, H.-K. Chung, R. Heeter, W. Hsing, J. A. Koch, H.-S. Park, H. F. Robey, H. A. Scott, R. Tommasini, J. Frenje *et al.*, Numerical simulation of thin-shell direct drive DHe3-filled capsules fielded at OMEGA, Phys. Plasmas **19**, 072702 (2012).

[17] E. S. Dodd, J. F. Benage, G. A. Kyrala, D. C. Wilson, F. J. Wysocki, W. Seka, V. Yu. Glebov, C. Stoeckl, and J. A. Frenje, The effects of laser absorption on direct-drive capsule experiments at OMEGA, Phys. Plasmas **19**, 042703 (2012).

[18] A. Pak, L. Divol, C. R. Weber, L. F. Berzak Hopkins, D. S. Clark, E. L. Dewald, D. N. Fittinghoff, V. Geppert-Kleinrath, M. Hohenberger, S. Le Pape *et al.*, Impact of Localized Radiative Loss on Inertial Confinement Fusion Implosions, Phys. Rev. Lett. **124**, 145001 (2020).

[19] R. E. Chrien, N. M. Hoffman, J. D. Colvin, C. J. Keane, O. L. Landen, and B. A. Hammel, Fusion neutrons from the gas-pusher interface in deuterated-shell inertial confinement fusion implosions, Phys. Plasmas **5**, 768 (1998).

[20] D. C. Wilson, P. S. Ebey, T. C. Sangster, W. T. Shmayda, V. Yu. Glebov, and R. A. Lerche, Atomic mix in directly driven inertial confinement implosions, Phys. Plasmas **18**, 112707 (2011).

[21] V. A. Smalyuk, R. E. Tipton, J. E. Pino, D. T. Casey, G. P. Grim, B. A. Remington, D. P. Rowley, S. V. Weber, M. Barrios, L. R. Benedetti, D. L. Bleuel, D. K. Bradley, J. A. Caggiano, D. A. Callahan, C. J. Cerjan, D. S. Clark, D. H. Edgell, M. J. Edwards, J. A. Frenje, M. Gatu-Johnson *et al.*, Measurements of an Ablator-Gas Atomic Mix in Indirectly Driven Implosions at the National Ignition Facility, Phys. Rev. Lett. **112**, 025002 (2014).

[22] M. B. Schneider, G. Dimonte, and B. Remington, Large and Small Scale Structure in Rayleigh-Taylor Mixing, Phys. Rev. Lett. **80**, 3507 (1998).

[23] P. E. Dimotakis, The mixing transition in turbulent flows, J. Fluid Mech. **409**, 69 (2000).

[24] T. J. Murphy, M. R. Douglas, J. R. Fincke, R. E. Olson, J. A. Cobble, B. M. Haines, C. E. Hamilton, M. N. Lee, J. A. Oertel, N. A. G. Parra-Vasquez *et al.*, Progress in the development of the MARBLE platform for studying thermonuclear burn in the presence of heterogeneous mix on OMEGA and the National Ignition Facility, J. Phys.: Conf. Ser. **717**, 012072 (2016).

[25] H. Peng, X. M. Zhang, X. Wei, W. Zheng, F. Jing, Z. Sui, D. Fan, and Z. Lin, Status of the SG-III solid state laser project, Proc. SPIE **3492**, 25 (1999).

[26] Z. R. Cao, S. Y. Liu, H. Y. Zhang, Y. K. Ding, Y. L. Bai, J. P. Zhao, B. Y. Liu, and X. H. Bai, Shen-Guang III core X-ray Framing Cameras, Acta Photonica Sinica **38**, 1881 (2009).

[27] R. Ramis, R. Schmalz, and J. Meyer-Ter-Vehn, MULTI—A computer code for one-dimensional multigroup radiation hydrodynamics, Comput. Phys. Commun. **49**, 475 (1988).

[28] M. Murakami, J. Meyer-Ter-Vehn, and R. Ramis, Thermal x-ray emission from ion-beam-heated matter, J. X-Ray Sci. Technol. **2**, 127 (1990).

[29] W. X. Li, *One-Dimensional Non-Steady Flow and Shock Waves* (National Defense Industry Press, Beijing, 2003), p. 278 (in Chinese).